JOURNAL OF APPLIED CRYSTALLOGRAPHY

ISSN: 1600-5767
journals.iucr.org/j

Determination of crystallographic texture in polycrystalline materials from wavelength-resolved neutron transmission experiments: application to high-symmetry crystals

Miguel Angel Vicente Alvarez, Florencia Malamud and Javier Roberto Santisteban

J. Appl. Cryst. (2023). **56**, 1721–1731

JOURNAL OF APPLIED CRYSTALLOGRAPHY
ISSN 1600-5767

Received 10 February 2023
Accepted 10 October 2023

Edited by T. J. Sato, Tohoku University, Japan

Keywords: crystallographic texture; wavelength-resolved neutron transmission; neutron cross section.

Determination of crystallographic texture in polycrystalline materials from wavelength-resolved neutron transmission experiments: application to high-symmetry crystals

Miguel Angel Vicente Alvarez,[a,b]* Florencia Malamud[c] and Javier Roberto Santisteban[a]

[a]Laboratorio Argentino de Haces de Neutrones, Centro Atómico Bariloche, Comisión Nacional de Energía Atómica, Avenida Bustillo 9500, Buenos Aires, Rio Negro 8400, Argentina, [b]Consejo Nacional de Investigaciones Científicas y Técnicas, Argentina, and [c]Laboratory for Neutron Scattering and Imaging, Paul Scherrer Institute, Forschungsstrasse 111, Villigen PSI, Switzerland. *Correspondence e-mail: m.a.vicente@cab.cnea.gov.ar

Wavelength-resolved neutron transmission experiments are useful for characterizing the microstructure of macroscopic specimens with 2D spatial resolution perpendicular to the beam direction. The crystallographic texture can affect the neutron transmission in the thermal neutron energy range, which manifests as changes in the shape and height of Bragg edges as a function of neutron wavelength. Models have been proposed to predict the transmission of textured polycrystalline materials from knowledge of the material texture and have proved to accurately predict the observed transmission data. In recent work, a novel method was described and tested for obtaining texture integral parameters from the combined analysis of transmission data measured along several directions of a specimen in a hexagonal crystal Zr alloy. However, this procedure has limitations when dealing with high-symmetry crystal structures. In this work, a generalization of such a method based on the expansion of the orientation distribution function (ODF) in symmetric generalized spherical harmonics that is applicable to all crystal and sample symmetries is presented. Using this method, the low-order Fourier coefficients of the ODF can be estimated by analyzing transmission data obtained for a reduced set of beam directions. This method was verified using a cubic Cu sample, for which transmission data were available along five different directions. Two sample symmetries were assumed to reduce the number of Fourier coefficients of the ODF. In the case of cylindrical symmetry (fiber-type texture), the results were good; but in the case of orthorhombic symmetry, some bias was observed which was attributed to the reduced number of beam directions used to perform the evaluation.

1. Introduction

Use of neutron transmission has advanced in recent years as a tool for characterizing the microstructure of materials with submillimetric 2D spatial resolution perpendicular to the beam direction (Woracek *et al.*, 2018). This has been made possible by taking advantage of the energy resolution of neutrons provided by time-of-flight techniques, the development of sound theoretical background (Santisteban *et al.*, 2001) and software development (Dollase, 1986; Vogel, 2000; Sato *et al.*, 2011; Dessieux *et al.*, 2019; Malamud *et al.*, 2023). Examples include 3D imaging (tomography) to quantify phase volumes inside samples (Woracek *et al.*, 2014; Carminati *et al.*, 2020; Sato *et al.*, 2021) and 2D imaging to characterize crystalline phase strains (Wensrich *et al.*, 2016; Su *et al.*, 2016, 2021) by analyzing the position of Bragg edges in transmission images.

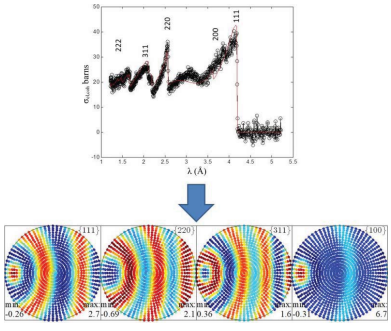

The recent advancements in energy resolution and acquisition time of neutron transmission experimental facilities have greatly facilitated the determination of crystallographic texture through energy-resolved neutron transmission experiments. This is achieved by analyzing the Bragg edges in the thermal neutron energy range. Neutron diffraction is a common method to determine the crystallographic texture in the interior of samples (Peterson *et al.*, 2021; Xu *et al.*, 2018; Takajo & Vogel, 2018; Onuki *et al.*, 2016). In contrast to neutron diffraction, which has a spatial resolution of several millimetres, neutron transmission experiments can achieve sub-millimetre resolution in transmission images. While neutron diffraction is a volumetric technique, the gauged volume in neutron transmission experiments traverses the entire sample thickness along the beam direction. Despite this limitation, neutron transmission still benefits from high spatial resolution, allowing the study of texture gradients that are difficult to measure by neutron diffraction.

On the other hand, neutron tomography can achieve excellent spatial resolution in the interior of objects, which is useful for studying the distribution of phases. However, obtaining spatial information about strain, particle size and orientation from neutron tomography is a more complex task (Watanabe *et al.*, 2019). Traditional reconstruction methods fail due to the directional nature of these parameters, resulting in a voxel within the sample having a cross section that varies with sample orientation. In traditional reconstruction methods, an isotropic total cross section is assumed, which remains constant for all orientations of the object explored using neutrons. It is clear that a better understanding of the transmission models is necessary to improve tomographic reconstruction capabilities in textured specimens.

The experimental determination of the transmitted wavelength-resolved neutron spectrum consists of measuring the spectroscopic transmission of the specimen $T(\lambda)$ by comparing the signal recorded on the detector when the sample is in the beam $i(\lambda)$ with the signal recorded for the direct neutron beam $i_0(\lambda)$:

$$T(\lambda, \boldsymbol{\tau}) = \frac{i(\lambda, \boldsymbol{\tau})}{i_0(\lambda)}, \tag{1}$$

where $\boldsymbol{\tau}$ indicates the direction of the transmitted neutron beam in the coordinate system of the sample. Within the kinematical theory of diffraction for polycrystalline materials, this transmission is directly related to the microscopic total cross section $\sigma_{\rm tot}(\lambda, \boldsymbol{\tau})$ of a unit cell of the material by

$$T(\lambda, \boldsymbol{\tau}) = \exp\left[-N_{\rm cell} h \sigma_{\rm tot}(\lambda, \boldsymbol{\tau})\right], \tag{2}$$

where h is the thickness of the specimen along the neutron beam direction and $N_{\rm cell}$ is the number of unit cells per unit volume. The total cross section includes all processes that remove neutrons from the incident beam (*i.e.* Bragg reflection, diffuse scattering and absorption). For the thermal/cold range, the absorption contribution $\sigma_{\rm A}(\lambda)$ is given by a linear increasing dependence with λ:

$$\sigma_A(\lambda) = \frac{\sigma_{\rm abs}\lambda}{\lambda_{\rm o}}, \tag{3}$$

where $\sigma_{\rm abs}$ is the microscopic absorption cross section of the atom at the wavelength $\lambda_{\rm o}$ [typically $\lambda_{\rm o}$ = 1.798Å (Luzin & Brokmeier, 2002)]. The diffuse scattering contribution $\sigma_{\rm s}(\lambda)$ includes a combination of incoherent scattering processes and inelastic scattering and, like $\sigma_{\rm A}(\lambda)$, is largely independent of the incident beam direction and has a smooth dependence on neutron wavelength. Theoretical expressions to calculate this contribution are given by Granada (1984) and can be found in the appendix of Malamud & Santisteban (2016).

The total cross section component attributed to the Bragg reflection $[\sigma_{\rm el,coh}(\lambda, \boldsymbol{\tau})]$ can be experimentally determined along the specific specimen direction $\boldsymbol{\tau}$ by extraction from the measured neutron transmission data $T(\lambda, \boldsymbol{\tau})$:

$$\sigma_{\rm el,coh}(\lambda, \boldsymbol{\tau}) = -\frac{1}{N_{\rm cell} h}\ln[T(\lambda, \boldsymbol{\tau})] - \sigma_{\rm s}(\lambda) - \sigma_{\rm A}(\lambda). \tag{4}$$

The coherent elastic term is the aspect of neutron total cross section affected by texture. In the case of polycrystalline materials with a small grain size (typically <5 µm), where the kinematic approximation of diffraction is good, a closed expression for the coherent elastic contribution in terms of integrals over the pole figures was proposed (Santisteban *et al.*, 2012). This expression was evaluated in materials with known texture and compared with experimental measurements for quite different crystal structures and crystallographic textures with good success (Santisteban *et al.*, 2012; Malamud *et al.*, 2014; Malamud, 2016). After these studies, it was shown that the integrals over the pole figures can be solved analytically when the orientation distribution function (ODF) is expressed as a Fourier decomposition in terms of the generalized spherical harmonic functions or its equivalent Wigner functions (Laliena *et al.*, 2020). This new equation enables a rapid evaluation of the transmission data for known ODFs.

A novel methodology was recently proposed to obtain integral parameters of the ODF by combining the transmission data obtained for different beam directions based on the Fourier decomposition of the ODF. This method was described in a recent paper by Vicente Alvarez *et al.* (2021) and is applicable to materials with spatially uniform texture. The proposed methodology relies on the expansion of $\sigma_{\rm el,coh}(\lambda, \boldsymbol{\tau})$ in terms of functions of λ, whose expansion coefficients depend only on the texture Fourier coefficients and the beam direction. The utility of this methodology lies in its ability to estimate the low-l Fourier coefficients of the ODF from the transmission data, which can then be used to evaluate the directional dependence of volume-averaged properties of the polycrystalline aggregate such as bulk electrical resistivity and elastic stiffness. This methodology was successfully applied to the case of Kearns factors in a textured Zr alloy (hexagonal close packed crystal structure) where the transmission was measured along only two beam directions. One necessary condition for the application of this method is the linear independence (LI) of the set of functions used to

expand $\sigma_{\mathrm{el,coh}}(\lambda, \boldsymbol{\tau})$. If the ODF is expanded using generalized spherical harmonics (or Wigner functions), this LI condition is not fulfilled due to crystal symmetry. In some cases, such as hexagonal crystal symmetry, the linearly dependent functions can be easily identified and eliminated, as explained by Vicente Alvarez *et al.* (2021). However, in high-symmetry crystals (*e.g.* cubic) this is not straightforward.

The objective of this study is to introduce a generalized version of the recent methodology for estimating Fourier coefficients of the ODF from transmission data, while ensuring the LI condition is automatically satisfied. This is achieved by expressing the ODF in terms of symmetrized generalized spherical harmonics, which were originally introduced by Bunge (1982) and account for both crystal and sample symmetries. In the following section, we derive the expression for $\sigma_{\mathrm{el,coh}}(\lambda, \boldsymbol{\tau})$ and outline the procedure for obtaining the Fourier coefficients of the ODF from transmission data. Section 3 explains how the instrumental resolution function is incorporated into the formalism. Then, in Section 4, we calculate $\sigma_{\mathrm{el,coh}}(\lambda, \boldsymbol{\tau})$ for a Cu sample with a known ODF and compare our results with experimental transmission measurements obtained at the ENGINX-ISIS neutron facility. In Section 5, we apply the inversion method to the same Cu sample (*i.e.* we obtain the Fourier coefficients from the experimental transmissions). Finally, in Section 6, we summarize the main findings and conclusions.

2. The model

In this section, we present the derivation of the Fourier expansion expression for the elastic coherent cross section as a function of neutron wavelength in the kinematic diffraction approximation. However, unlike in our previous work (Vicente Alvarez *et al.*, 2021), here we express this quantity in terms of symmetrized functions that comply with the crystal and sample symmetry. This approach enables us to directly expand the elastic coherent cross section in terms of a set of independent functions whose coefficients are linked to the Fourier coefficients of the ODF of the sample. Since these sets of functions are independent by definition, carrying out the inversion of the linear system to obtain the expansion coefficients is straightforward.

The neutron coherent elastic cross section $\sigma_{\mathrm{el,coh}}$ of a textured polycrystal in the kinematic approximation is given by

$$\sigma_{\mathrm{el,\,coh}}(\lambda, \boldsymbol{\tau}) = \frac{N(2\pi)^3}{v_0} \sum_{\mathbf{G}} \left[\left|F_{\mathbf{G}}\right|^2 \oint\!\!\int f(g)\delta(\mathbf{k}' - \mathbf{k} - g\mathbf{G})\, \mathrm{d}g\, \mathrm{d}\Omega_{k'} \right], \tag{5}$$

where $\lambda = 2\pi/k$ is the neutron wavelength, $\boldsymbol{\tau}$ is the direction of the incident beam in the sample reference system, $\mathbf{k} = k\boldsymbol{\tau}$, N is the number of crystals cells along the section traversed by the beam and v_0 is the volume of the crystal cells. Summation is done over all reciprocal lattice vectors $\mathbf{G}$ with the structure factor $F_{\mathbf{G}}$. The first integral is taken over all crystal orientations g, with $f(g)$ being the ODF representing the texture. The second integral is over all exit directions of the neutrons that suffer elastic diffraction in the crystal with the orientation $g = (\varphi_1, \phi, \varphi_2)$. Note that in this work we follow the same convention for the definition of rotations and angles as proposed by Bunge (1982).

Following Bunge (1982), $f(g)$ can be expanded in a series of symmetrized generalized spherical harmonics $T_{l\mu\nu}^{\mathrm{CS,SS}}$:

$$f(g) = \sum_{l=0} \sum_{\mu=1}^{M(l)} \sum_{\nu=1}^{N(l)} C_{l\mu\nu} T_{l\mu\nu}^{\mathrm{CS,SS}}(g), \tag{6}$$

where CS and SS refer to crystal and sample symmetries, respectively; $C_{l\mu\nu}$ are the Fourier coefficients; and summations run from 1 to $M(l)$ and to $N(l)$.

The $T_{l\mu\nu}^{\mathrm{CS,SS}}$ functions are evaluated as a linear combination of the non-symmetrized generalized spherical harmonics T_{lmn}:

$$T_{l\mu\nu}^{\mathrm{CS,SS}}(g) = \sum_{m=-l}^{l} \sum_{n=-l}^{l} S_{l,m\mu}^{\mathrm{CS}} S_{l,n\nu}^{\mathrm{SS}} T_{lmn}(g). \tag{7}$$

The T_{lmn} functions are a generalization of the associated Legendre functions, defined in chapter 14 of Bunge (1982), where the coefficients $S_{l,m\mu}^{\mathrm{CS}}$ and $S_{l,n\nu}^{\mathrm{SS}}$ depend on the crystal and sample symmetries, respectively. The definition of $S_{l,m\mu}^{\mathrm{CS}}$ coefficients for hexagonal, orthorhombic, tetragonal and cylindrical symmetries can be found in Table 14.4 of Bunge (1982), and for cubic symmetry in Table 15.2.2 of Bunge (1982), or Morris (1995) and Muggli (1972).

In this context, it is important to highlight the advantages of using symmetrized functions. Firstly, using symmetrized functions allows the Euler space to be reduced to the fundamental region. Secondly, the total number of functions $T_{l\mu\nu}^{\mathrm{CS,SS}}$ required to expand the ODF is drastically reduced compared with the non-symmetrized case. In the non-symmetrized case, for each l, this number increases as $(2l + 1)^2$.

Substituting equations (6) and (7) into (5) and following the procedure described in Appendix *C* of Laliena *et al.* (2020), the following expression can be obtained for the elastic cross section:

$$\sigma_{\mathrm{el,coh}}(\lambda, \boldsymbol{\tau}) = \frac{N(2\pi)^3}{v_0 k^3} \sum_{\mathbf{G}} \frac{k}{2G} \left|F_{\mathbf{G}}\right|^2 \theta\left(1 - \frac{G}{2k}\right) \times \sum_{\substack{l=0\ldots \\ \mu=1\ldots M(l) \\ \nu=1\ldots N(l)}} k_{l\mu}^{\mathrm{CS}}(\hat{\mathbf{G}}) k_{l\nu}^{\mathrm{SS}^*}(\boldsymbol{\tau}) \frac{4\pi}{2l+1} P_l\left(\frac{G}{2k}\right) C_{l\mu\nu}, \tag{8}$$

where P_l refers to Legendre polynomials. The asterisk refers to complex conjugate, and the functions $k_{l\mu}^{\mathrm{CS}}$ and $k_{l\nu}^{\mathrm{SS}}$ are the symmetrized versions of the surface spherical harmonics $k_l^m(\hat{\mathbf{x}})$ for the crystal and sample symmetries, respectively. These functions are given by

$$k_{l\mu}^{\mathrm{CS}}(\hat{\mathbf{x}}) = \sum_{m=-l}^{l} S_{l,m\mu}^{\mathrm{CS}} k_l^m(\hat{\mathbf{x}}). \tag{9}$$

Analogously to the approach presented by Vicente Alvarez *et al.* (2021), we express equation (8) as the product of two terms: **B**, which solely depends on the neutron wavelength λ, and **A**,

which only relies on the neutron beam direction in the sample reference system:

$$\sigma_{\mathrm{el,coh}}(\lambda,\boldsymbol{\tau}) = \sum_{l=0}^{\infty}\sum_{\mu=1}^{M(l)} B_{l\mu}^{\mathrm{CS}}(\lambda) A_{l\mu}^{\mathrm{SS}}(\boldsymbol{\tau}), \tag{10a}$$

where

$$B_{l\mu}^{\mathrm{CS}}(\lambda) = \frac{2N(2\pi)^4}{v_0 k^3}\sum_{\mathbf{G}}\frac{k}{2G}\left|F_{\mathbf{G}}\right|^2\theta\left(1-\frac{G}{2k}\right)\frac{1}{2l+1} \times P_l\left(\frac{G}{2k}\right)k_{l\mu}^{\mathrm{CS}}(\hat{\mathbf{G}}) \tag{10b}$$

and

$$A_{l\mu}^{\mathrm{SS}}(\boldsymbol{\tau}) = \sum_{\nu=1}^{N(l)} C_{l\mu\nu} k_{l\nu}^{\mathrm{SS}^*}(\boldsymbol{\tau}). \tag{10c}$$

As previously explained by Vicente Alvarez *et al.* (2021), when considering a fixed beam direction, equation (10*a*) can be interpreted as an expansion of $\sigma_{\mathrm{el,coh}}(\lambda,\boldsymbol{\tau})$ as a linear combination of $B_{l\mu}^{\mathrm{CS}}(\lambda)$ functions, where the expansion coefficients correspond to the values of $A_{l\mu}^{\mathrm{SS}}(\boldsymbol{\tau})$ for each set of (l,μ). One of the main advantages of the present formalism is that the $B_{l\mu}^{\mathrm{CS}}(\lambda)$ functions are independent by construction, allowing for a straightforward inversion of equation (10*a*) to obtain the $A_{l\mu}^{\mathrm{SS}}(\boldsymbol{\tau})$ parameters from the experimental data.

From equations (10*a*), (10*b*) and (10*c*), it is also straightforward to evaluate the dependence of the height of the Bragg edge on the texture. The edge height corresponding to the (*hkl*) plane with *d* spacing d_{hkl} is given by the difference $t_{hkl} = \sigma_{\mathrm{el,coh}}(\lambda^-,\boldsymbol{\tau}) - \sigma_{\mathrm{el,coh}}(\lambda^+,\boldsymbol{\tau})$ with $\lambda^{\pm} = 2d_{hkl} \pm \delta$, where δ is infinitesimally small. From equation (10*a*) this is given by

$$t_{hkl}(\boldsymbol{\tau}) = \frac{2N(2\pi)^4}{v_0 k^3}\sum_{\mathbf{G}\ \text{with}\ G=2\pi/d_{hkl}}\left|F_{\mathbf{G}}\right|^2 \times \sum_{l,\mu,\nu}\frac{1}{2l+1}C_{l\mu\nu}k_{l\mu}^{\mathrm{CS}}(\hat{\mathbf{G}})k_{l\nu}^{\mathrm{SS}^*}(\boldsymbol{\tau}), \tag{11}$$

where we made use of $P_l(1) = 1$ for all l. The summation over l,μ,ν yields $\mathrm{PF}_{\hat{\mathbf{G}}}(\boldsymbol{\tau})/4\pi$, where $\mathrm{PF}_{\hat{\mathbf{G}}}(\boldsymbol{\tau})$ represents the pole figure intensity along direction $\boldsymbol{\tau}$ corresponding to the reciprocal vector $\hat{\mathbf{G}}$. Then equation (11) becomes

$$t_{hkl}(\boldsymbol{\tau}) = \frac{N(2\pi)^3}{v_0 k^3}\sum_{\mathbf{G}\ \text{with}\ G=2\pi/d_{hkl}}\left|F_{\mathbf{G}}\right|^2\mathrm{PF}_{\hat{\mathbf{G}}}(\boldsymbol{\tau}). \tag{12}$$

The dependence of the Bragg edge height occurring at a specific *d* spacing d_{hkl} on the beam direction $\boldsymbol{\tau}$ is proportional to the weighted sum of the structure factor $\left|F_{\mathbf{G}}\right|^2$ over all pole figures of reciprocal vectors $\hat{\mathbf{G}}$ with the modulus $G = 2\pi/d_{hkl}$. In the case where the distance d_{hkl} depends only on the permutation of the Miller indices (*hkl*), the summation reduces to the multiplicity of the plane.

3. Comparison with experimental data

In a time-of-flight (TOF) experiment, the shape of $\sigma_{\mathrm{el,coh}}(\lambda,\boldsymbol{\tau})$ with λ depends on the instrumental resolution function, which takes into account all experimental errors contributing to the uncertainty in the arrival time of the neutron (t). This function is defined by the average time spent by the neutrons within the moderator (emission time t_e) and the time taken by the neutron to travel to the detector ($t_L = mL\lambda/h$, where m is the neutron mass, L is the length travelled by the neutron and h is Planck's constant). Malamud & Santisteban (2016) proposed a simple expression for this function:

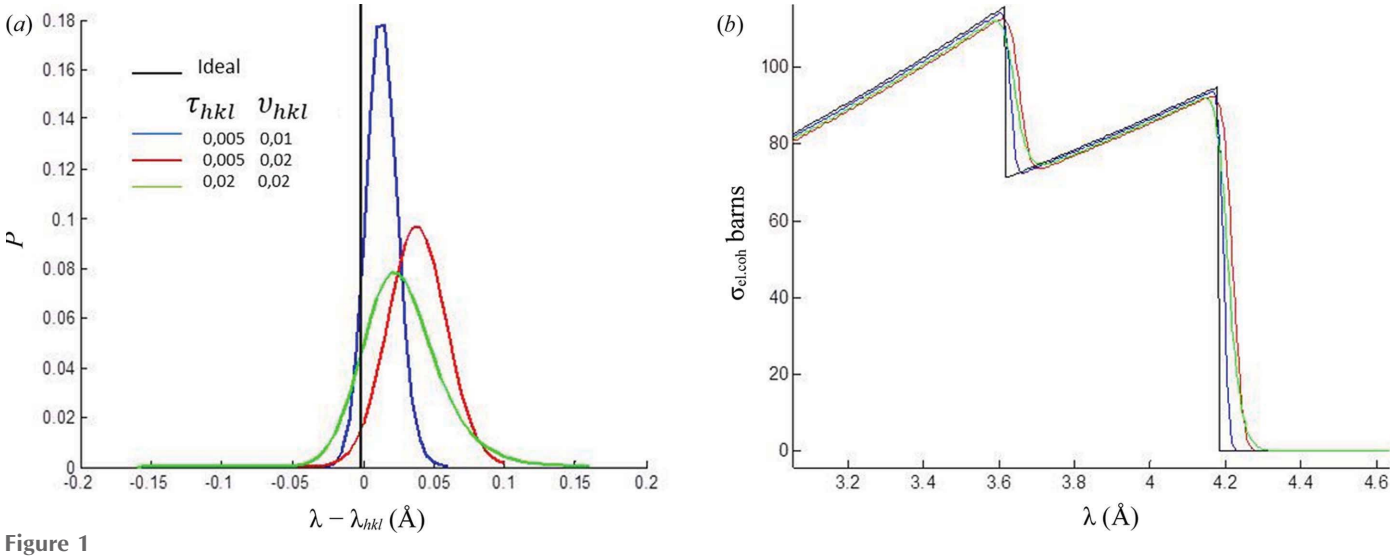

Figure 1
(*a*) Normalized instrumental resolution functions (*P*) for different values of τ_{hkl} and υ_{hkl}. (*b*) Calculated $\sigma_{\mathrm{el,coh}}$ for a Cu powder sample after convolution of equations (10*a*) and (13) using the different instrumental resolution functions from (*a*).

$$P\left[\lambda_{hkl}, (\tau_{hkl}, \upsilon_{hkl}), \lambda\right] = \frac{A(\tau_{hkl}, \upsilon_{hkl})}{2\tau_{hkl}} \exp\left(-\frac{\lambda-\lambda_{hkl}}{\tau_{hkl}} + \frac{{\upsilon_{hkl}}^2}{2{\tau_{hkl}}^2}\right) \times \operatorname{erfc}\left(-\frac{\lambda-\lambda_{hkl}}{\sqrt{2}\upsilon_{hkl}} + \frac{\upsilon_{hkl}}{\tau_{hkl}}\right), \quad (13)$$

where λ_{hkl} is the wavelength in the ideal case and λ represents the deviation from this ideal value. This function is asymmetric and arises from the convolution of an exponential function with constant τ_{hkl} and a Gaussian function of width υ_{hkl} as explained in the literature (Malamud & Santisteban, 2016). The constant $A(\tau_{hkl}, \upsilon_{hkl})$ is a normalization factor. In principle, the values of τ_{hkl} and υ_{hkl} depend on λ_{hkl}. Some examples of function P are presented in Fig. 1(*a*), together with the ideal case, which is represented as a delta function centered at $\lambda = \lambda_{hkl}$. To compare the theoretical result with the experimental data, it is necessary to convolve the theoretical function for $\sigma_{\mathrm{el,coh}}(\lambda, \boldsymbol{\tau})$ as given in equation 10(*a*) with the function P from equation (13). In the context of this methodology, this is equivalent to convolution of all $B_{l\mu}^{\mathrm{CS}}(\lambda)$ functions of equation (10*b*) with P given by equation (13).

Fig. 1(*b*) presents the results of calculations performed for a Cu sample (face-centered cubic, lattice parameter 3.6149 Å), where the powder contribution to the total elastic cross section $\sigma_{\mathrm{el,coh}}(\lambda, \boldsymbol{\tau})$ was evaluated using the function $B_{01}^{\mathrm{CS}}(\lambda)$ for different instrumental functions, as shown in Fig. 1(*a*). In the 'ideal' case, where the instrumental resolution is a delta function, the powder contribution displays sharp discontinuities at the Bragg edge positions λ_{hkl}. For the other three cases, the shape of the discontinuity exhibits a smoother dependence for neutron wavelengths higher than λ_{hkl}. Additionally, the edge is shifted to higher values of λ, as the maximum of the instrumental distribution function occurs at values of $\lambda - \lambda_{hkl} > 0$.

4. Evaluation of the elastic cross section from a known ODF

To evaluate the coherent elastic cross section using equation (10*a*) from a known ODF, it is necessary to calculate the symmetrized version of the Fourier coefficients $C_{l\mu v}$. However, these coefficients are generally not available in common texture analysis software. In the free MATLAB toolbox for texture analysis *MTEX* (Hielscher & Schaeben, 2008), the non-symmetrized Fourier coefficients are readily available. These coefficients are defined for Wigner functions D_{lmn}, which use a different sequence of rotations (zyz) to define orientations compared with the notation used by Bunge (1982) (zxz) in the definition of T_{lmn} functions. Nevertheless, it is simple to compute the Fourier coefficients of functions T_{lmn} from those provided by *MTEX* for the D_{lmn} functions. Finally, the symmetrized Fourier coefficients $C_{l\mu v}$ can be obtained from the non-symmetrized version C_{lmn} using

$$C_{l\mu v} = \sum_{\substack{m=-l \\ n=-l}}^{l} S_{l,m\mu}^{\mathrm{CS}} S_{l,nv}^{\mathrm{SS}} C_{lmn}. \quad (14)$$

We compared the total coherent elastic cross section given by equation (10*a*) with measurements performed on a textured sample of Cu. The specimen of ~20 × 20 × 10 mm, shown in Fig. 2(*a*), was produced as a reference to compare its texture with prehistoric copper axes (Artioli, 2007). The ODF of the sample was determined by neutron diffraction measurements at room temperature with the ENGIN-X diffractometer (Santisteban *et al.*, 2006) with a 6 × 6 × 2 mm gauge volume, and data processing was done using the *NyRTex* texture analysis routine (Malamud *et al.*, 2014). The sample reference system was defined by the ND (normal to the sample surface), whereas the transverse and longitudinal directions (TD and LD) were arbitrarily chosen with respect to the sample holder (see Fig. 2). In the pole figures, the ND corresponds to the center of the figures, and the TD and LD to the east and north, respectively. The color scales of these pole figures are different from one another and go from the lowest value in blue to the highest value in red. The texture presents a marked (200) fiber due to columnar grain growth during crystallization. The direction of this fiber is some degrees shifted from the TD as displayed in the (111), (200), (220) and (211) pole figures of Fig. 2(*b*). For some specific beam directions, the transmission data were also collected by a detector located behind the sample. These TOF spectra were measured simultaneously with the diffraction pattern at ENGIN-X, with an incident beam divergence of ~0.5°. The exposed beam directions are identified as white squares in the (200) pole figure of Fig. 2(*b*) and were labeled from 1 to 5.

The coherent elastic cross section $\sigma_{\mathrm{el,coh}}(\lambda, \boldsymbol{\tau})$ was obtained from neutron transmission measurements by subtracting the inelastic and absorption components using equation (4), and converting the time-of-flight (TOF) to neutron wavelength. Fig. 3 displays the experimental $\sigma_{\mathrm{el,coh}}(\lambda, \boldsymbol{\tau})$ per crystal cell for beam directions 1 and 3 as hollow black circles. Note that, for

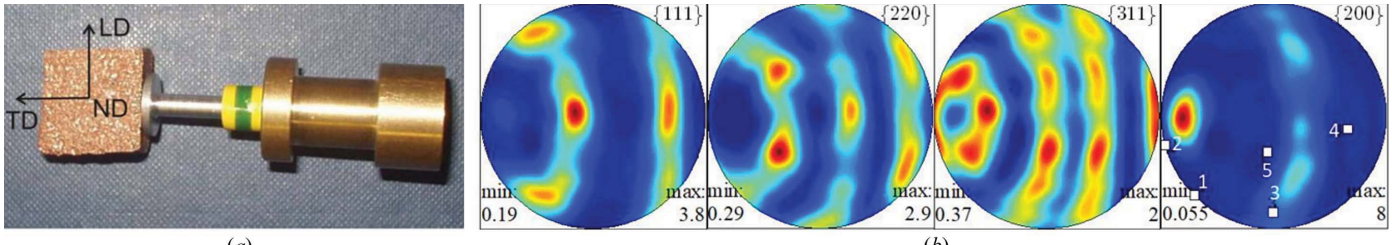

(*a*) (*b*)

Figure 2
(*a*) Sample with its holder. (*b*) Crystallographic texture of the Cu sample. The white squares in the (200) pole figures indicate the direction of the incident beam in the transmission experiment.

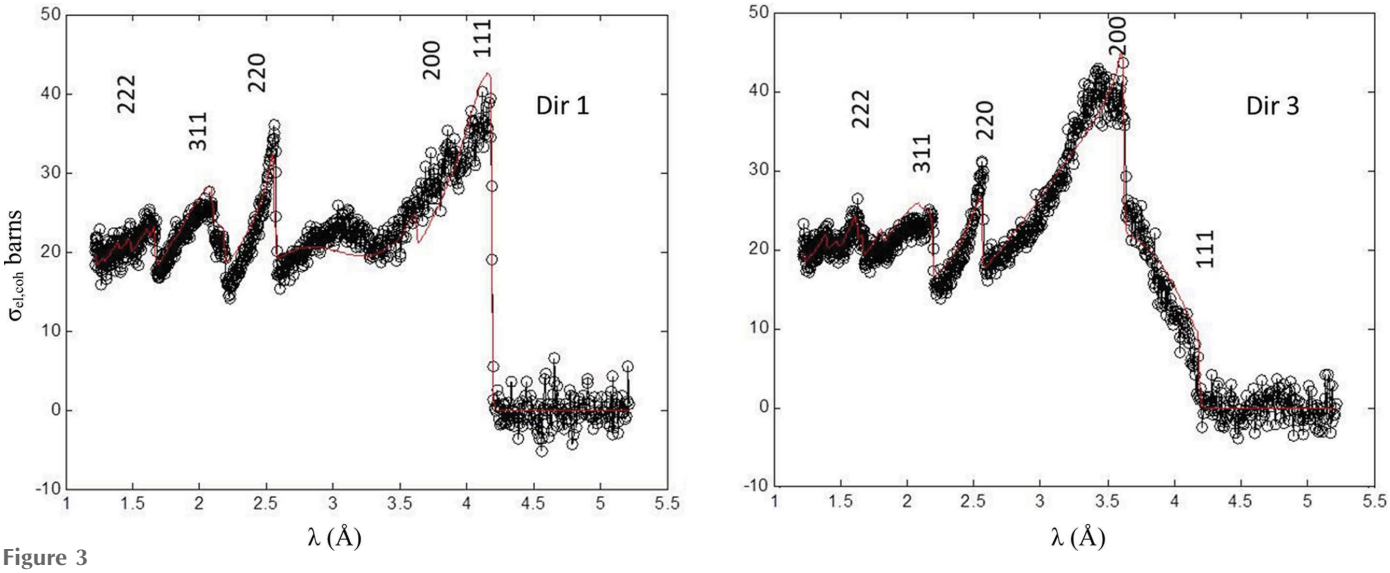

Figure 3
Elastic cross section measured for the Cu sample for two directions (white circles) and calculated using the ODF result of Fig. 2(*b*) as initial input data (red lines).

values of λ greater than 4.2 Å, there is no elastic contribution to the total neutron cross section, and the Bragg edges corresponding to the first diffraction planes are indicated in the figures. The shape of the elastic cross section differs between the two beam directions due to the sample texture. To define the instrumental resolution function we assumed constant values of τ_{hkl} = 0.02 Å and υ_{hkl} = 0.02 Å for all *hkl*. The Debye–Waller factor was calculated using a mean square of atomic displacement of $\langle u^2 \rangle$ = 0.0075 Å^2, and the scattering length of Cu atoms was taken to be 7.718 barns (Sears & Shelley, 1991).

We conducted simulations in the 1–6 Å wavelength range, with 0.001 Å steps for the five different beam directions. The red lines overlaid on the figures represent the evaluation of equation (10*a*) using the Fourier coefficients obtained from the ODF of Fig. 2. For direction 3, there is a good agreement between the experimental elastic cross section measured using the neutron transmission method and the simulated theoretical elastic cross section using the ODF result of Fig. 2(*b*) as initial input data across the entire wavelength range, with the theoretical values almost overlapping the experimental ones. For direction 1, the agreement is satisfactory, except for minor differences in the Bragg edges 111 and 200. These differences can be attributed to either small misalignments of this point with respect to the sample coordinate system or possible differences in the actual ODF from the measured one in the vicinity of direction 1. Similar outcomes are seen for directions 2, 4 and 5.

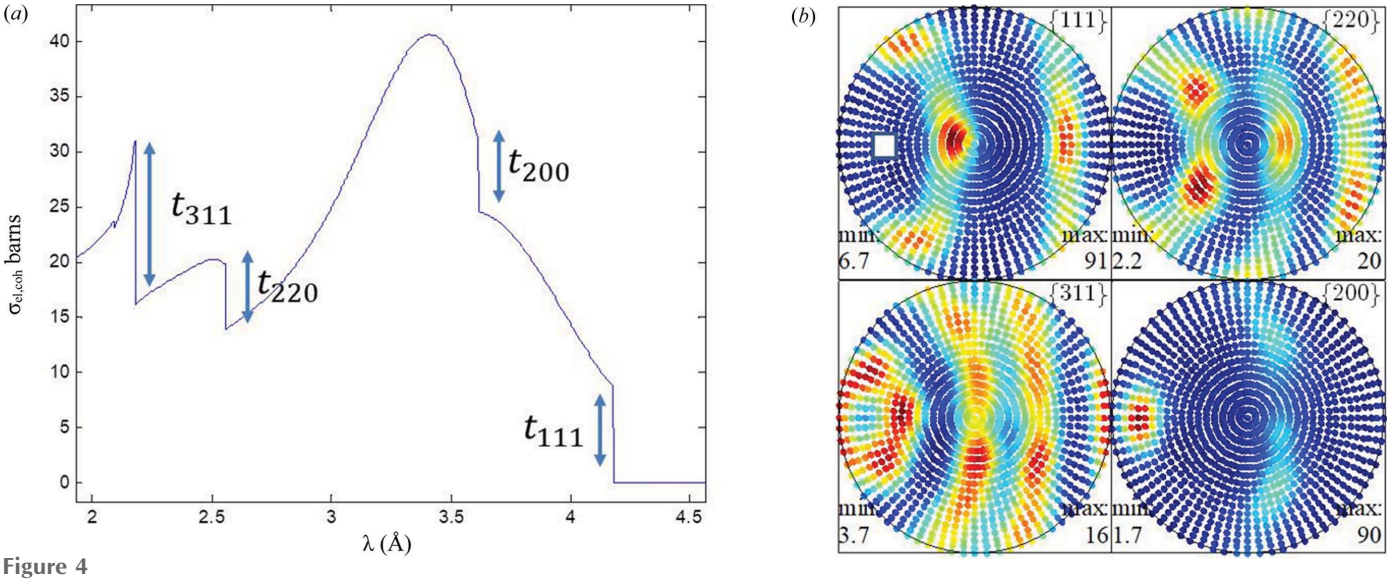

Figure 4
Simulation of the variations in the height of four Bragg edges as a function of beam direction for the Cu specimen using the ODF result of Fig. 2(*b*) as initial input data. (*a*) Example transmission spectrum, where the Bragg edge heights (t_{hkl}) are indicated with the arrows. This transmission spectrum corresponds to the beam direction indicated as a white square in the (111) pole figure of (*b*). (*b*) Results of the simulations plotted as pole figures.

The variations of the Bragg edge height for different planes as a function of beam direction provide an interesting feature worth exploring. As discussed in the previous section and summarized in equation (12), the height dependence on the beam direction is proportional to the pole figure of the corresponding plane. To verify this relationship, a sequence of 2592 beam directions was simulated, covering the entire solid angle in a mesh of 5 × 5° steps. Fig. 4(*a*) shows a typical $\sigma_{\mathrm{el,coh}}$ obtained for a specific beam direction. For each spectrum, the heights t_{hkl} of the Bragg discontinuities associated with the (111), (200), (220) and (311) planes were stored and plotted as pole figures in Fig. 4(*b*). The color scales of these pole figures range from blue (lowest values) to red (highest values) in barns. Remarkably, these pole figures are identical to those in Fig. 2(*b*), thereby validating our proposed expressions and methodology.

5. Implementation of the inversion model

Considered as a function of wavelength, equation (10*a*) can be interpreted as a linear expansion of the coherent elastic scattering cross section, $\sigma_{\mathrm{el,coh}}(\lambda, \boldsymbol{\tau})$, in terms of the $B_{l\mu}^{\mathrm{CS}}(\lambda)$ functions, with $A_{l\mu}^{\mathrm{SS}}(\boldsymbol{\tau})$ coefficients. As the $B_{l\mu}^{\mathrm{CS}}(\lambda)$ functions have LI, the $A_{l\mu}^{\mathrm{SS}}(\boldsymbol{\tau})$ coefficients are uniquely determined. Therefore, for each spectrum measured for a given beam direction $\boldsymbol{\tau}$, there is a set of coefficients $A_{l\mu}^{\mathrm{SS}}(\boldsymbol{\tau})$ that can be easily obtained by a least-squares linear inversion method. Similarly, for each pair (l, μ), equation (10*c*) can be interpreted as a linear system for the unknowns $C_{l\mu\nu}$, where both $A_{l\mu}^{\mathrm{SS}}(\boldsymbol{\tau})$ and $k_{l\nu}^{\mathrm{SS}^*}(\boldsymbol{\tau})$ are already given.

The proposed inversion method, originally presented by Vicente Alvarez *et al.* (2021) and extended in this work, is a two-step procedure: first, the $A_{l\mu}^{\mathrm{SS}}(\boldsymbol{\tau})$ coefficients are determined from the measured elastic cross section spectra for the directions $\boldsymbol{\tau}_1, \boldsymbol{\tau}_2, \ldots$ Second, the linear system of equation (10*c*) is inverted to determine the Fourier coefficients $C_{l\mu\nu}$.

Table 1
Number of real Fourier coefficients of an ODF according to its sample symmetry for cubic crystals.

The number of scanned beam directions ($\boldsymbol{\tau}$) is indicated at the bottom as a reference.

Sample symmetry	$l = 0$	$l = 4$	$l = 6$	$l = 8$
Triclinic	1	9	13	17
Orthorhombic	1	3	4	5
Cylindrical	1	1	1	1
No. of available $A_{l\mu}^{\mathrm{SS}}$	5	5	5	5

It is clear from equation (10*c*) that the minimum number of beam directions necessary to have an invertible system is $N(l)$, which increases with the order l and depends on the sample symmetry. For example, for triclinic sample symmetry, $N(l) = 2l + 1$, whereas for cylindrical symmetry, $N(l) = 1$ for all l. Table 1 shows the values of $N(l)$ for different sample symmetries, and the number of beam directions required to determine the full texture for the case of the Cu sample is indicated at the bottom of the table. If the sample symmetry is triclinic, as in the case of the pole figures shown in Fig. 2, only the Fourier coefficients with $l = 0$ will be accessible with the five beam directions explored. Therefore, some assumptions regarding the sample symmetry must be made to apply the inversion method.

The inversion method was implemented in MATLAB. After the first step, $A_{l\mu}^{\mathrm{SS}}(\boldsymbol{\tau})$ coefficients were obtained from the experimental data for the five beam directions. Fig. 5 shows a comparison between the experimental measurements of $\sigma_{\mathrm{el,coh}}(\lambda, \boldsymbol{\tau})$ (black points) and the expansion in terms of functions $B_{l\mu}^{\mathrm{CS}}(\lambda)$ (red line) for directions 1 and 3. For the other directions similar results are obtained, where the curves corresponding to the series expansion lie on top of the experimental data. The curves shown in Fig. 5 correspond to $L_{\max} = 30$ for the series expansion of equation (10*a*).

The bottom of Fig. 5 shows the residuals, which are relatively small. Fig. 6(*a*) presents the sum of residuals as a

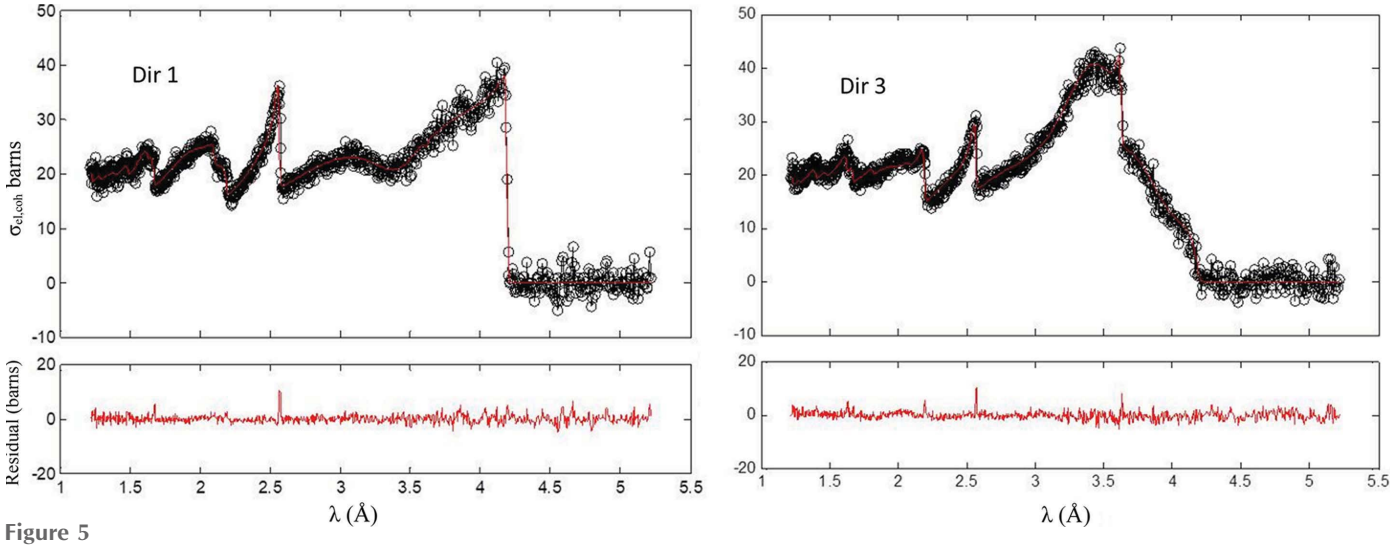

Figure 5
Comparison between the experimental elastic cross section data (black open circles) and the fitted elastic cross section data using the inverse model proposed here (red) for two beam directions.

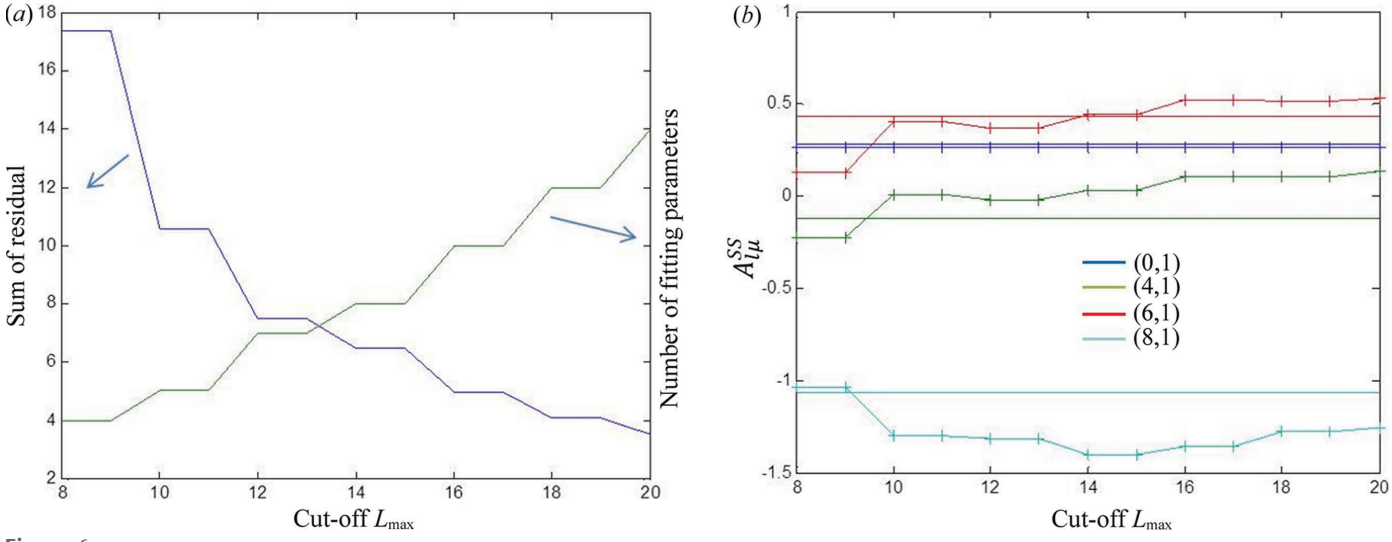

Figure 6
(*a*) Sum of residuals (blue line) and the number of fitting parameters (green) as a function of L_{max} [cut-off value of the series expansion of l in equation (10*a*)]. (*b*) Value of $A_{l\mu}^{SS}$ coefficients with $l \leq 8$ as a function of L_{max}. Each color corresponds to a different pair (l, μ). These curves correspond to the measurement of point 5.

function of L_{max} for direction 3. In Fig. 6(*b*) the dependence of the expansion coefficient $A_{l\mu}^{SS}(\boldsymbol{\tau})$ for (l, μ) equal to (0, 1), (4, 1), (6, 1) and (8, 1) on L_{max} is shown. The horizontal lines in the figure correspond to the values expected for these coefficients evaluated from the ODF measured by diffraction. The values of $A_{l\mu}^{SS}(\boldsymbol{\tau})$ obtained from the present method vary moderately with L_{max} and there is a good correspondence between the values obtained by the present method and those expected from equation (10*c*) using the Fourier coefficients of the ODF of Fig. 2. The small differences between them are ascribed to heterogeneities in the sample and differences in the volumes gauged by the diffraction and transmission determinations of the ODF, which are also reflected as the small differences between the experimental and estimated values of $\sigma_{el,coh}(\lambda, \boldsymbol{\tau})$ from the ODF observed in Fig. 3.

Table 1 indicates that, with only five beam directions, it is not possible to invert the linear system of equation (10*c*) for $l > 0$ without making additional assumptions. To address this, we propose two solution paths: (1) Orient the ODF of Fig. 2 in a way that places the intense (200) pole at the center of the pole figure, which allows us to assume some higher sample symmetry. (2) Assume that the texture is fiber-like with an unknown fiber direction and develop a minimization methodology that includes fitting for the fiber direction.

To implement the first solution path, we rotated the ODF accordingly. Fig. 7(*a*) shows the rotated pole figures and the new beam direction (rotated as the ODF). It is evident that, in this new reference system, the texture of the sample has either cylindrical or orthorhombic symmetry. We then applied the inversion of equation (10*c*) to estimate Fourier coefficients of the ODF for $l \leq 8$, assuming cylindrical or orthorhombic sample symmetry. With these coefficients, we calculated a truncated ODF and corresponding pole figures, presented in Fig. 7(*b*) for cylindrical and Fig. 7(*c*) for orthorhombic sample symmetries.

The results for cylindrical symmetry are quite promising, with the main texture components being reproduced well in terms of both intensity and angular position. However, for orthorhombic sample symmetry, the results are not as good. Although the intense (200) pole at the center is well reproduced and the fourfold structures of (111), (220) and (311) are present, negative values of the pole figures and ghost components are observed. These discrepancies can be attributed to errors in the determination of Fourier coefficients. In the case of cylindrical symmetry, only one coefficient is defined for each pair (l, μ) using five different values of $A_{l\mu}^{SS}(\boldsymbol{\tau})$. However, for orthorhombic symmetry, the linear system is almost a square system of equations for $l = 6$ and $l = 8$. Thus, even a small bias in the determination of $A_{l\mu}^{SS}(\boldsymbol{\tau})$ coefficients can have a significant impact on the estimated Fourier coefficients of the ODF.

The second solution path assumes that the sample texture is fiber-like, meaning it is axisymmetric for rotation along the fiber direction. However, the orientation of the fiber axis is unknown and needs to be determined using the experimental data. In the reference system normal to the fiber axis, there is only one Fourier coefficient different from zero for each pair (l, μ) up to $l \leq 8$. Thus, there are a total of six fitting parameters, including two angles and four Fourier coefficients (l = 0, 4, 6 and 8), whereas there are 20 experimental values of $A_{l\mu}^{SS}(\boldsymbol{\tau})$ (five for each value of l).

One complication of this method is that the system to be inverted in equation (10*c*) becomes nonlinear, which reduces the effectiveness of the minimization method. Fig. 8 presents a comparison between (1) the ODF of Fig. 2 truncated to L_{max} = 8 and assuming cylindrical symmetry and (2) the ODF obtained by the inversion method. The inversion method was able to capture the location of the fiber and the relative intensity of the different poles. However, some small differences were found, such as an overestimation of the intensity of

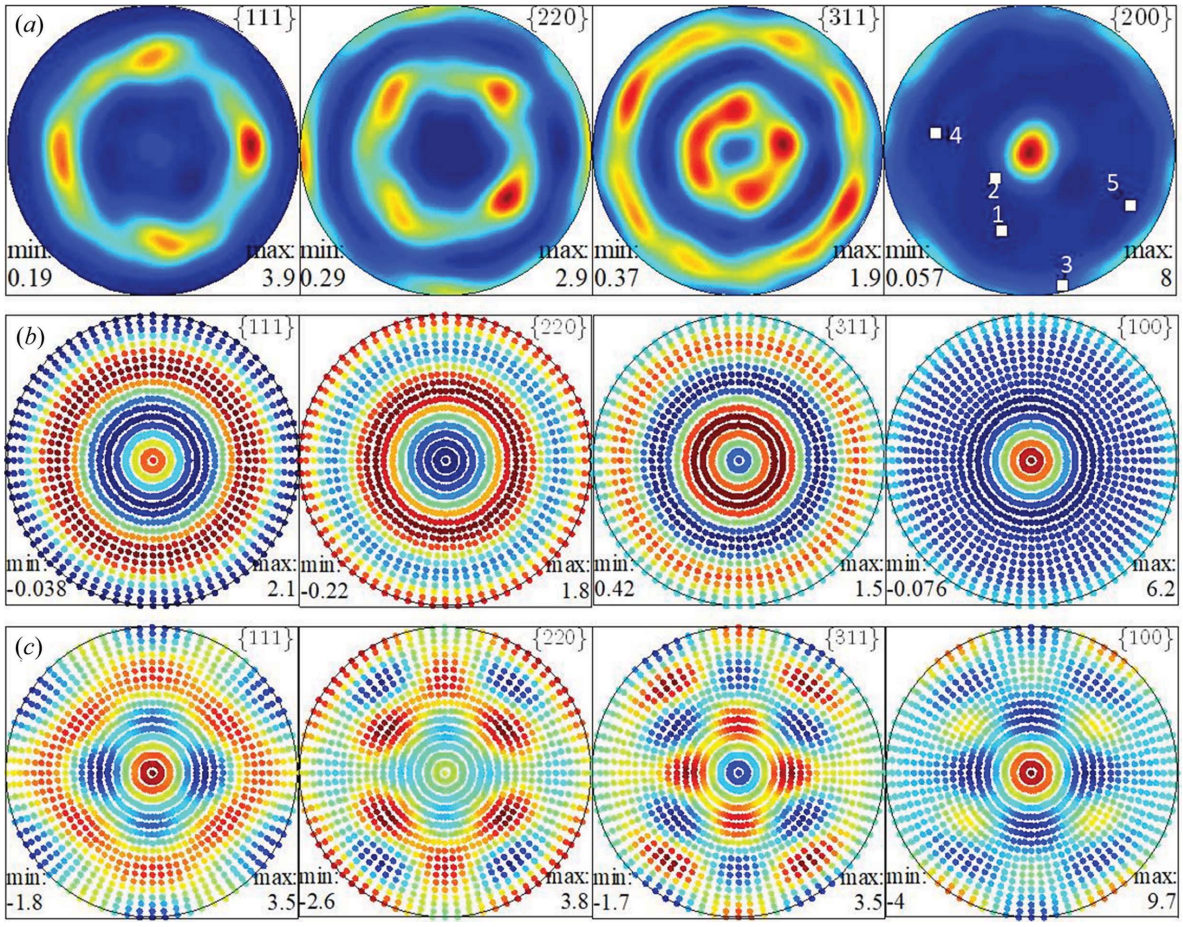

Figure 7
(*a*) Experimental pole figures measured using neutron diffraction obtained from a convenient rotation of Fig. 2(*b*). (*b*), (*c*) Estimated pole figures obtained from neutron transmission data after applying the inversion method proposed in this work (*b*) after assuming cylindrical sample symmetry considering only terms with $l \leq 8$ and (*c*) after assuming orthorhombic sample symmetry.

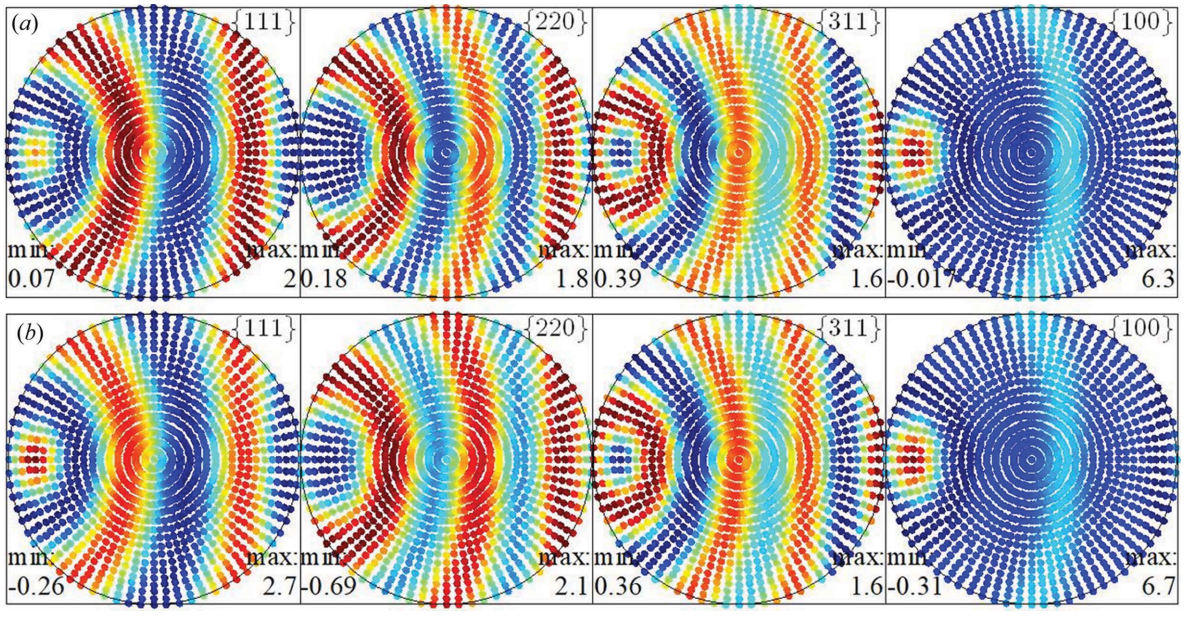

Figure 8
Pole figures in the approximation of fiber texture (*a*) calculated from the ODF of Fig. 2 and (*b*) estimated by the inversion method.

the (111) pole closest to the east of the pole figure, and some negative values due to errors in the determination of the $A_{l\mu}^{SS}(\boldsymbol{\tau})$ coefficients.

6. Conclusions

A two-step inversion procedure was developed to extract the Fourier coefficients of the ODF from energy-resolved neutron transmission spectra. This method utilizes an expression for the total coherent elastic cross section of textured polycrystals, which considers both sample and crystal symmetries, and is valid under the kinematic approximation of diffraction. The neutron wavelength and direction dependencies are decoupled, with the crystal structure being represented by the linearly independent $B_{l\mu}^{CS}(\lambda)$ functions, while the texture of the material is captured through its Fourier coefficients and the sample symmetry, represented by the $A_{l\mu}^{SS}(\boldsymbol{\tau})$ functions.

To verify the proposed method, we applied it to a Cu sample for which the texture was known from neutron diffraction experiments. The instrumental resolution was taken into account by convolving the $B_{l\mu}^{CS}(\lambda)$ functions with the instrumental resolution function, resulting in excellent agreement between the experimental data and the model for all five beam directions explored.

The two-step inversion procedure was then applied to the same Cu sample, where the experimental elastic cross section spectra were first expressed as a linear combination of $B_{l\mu}^{CS}(\lambda)$ functions with the linear coefficients being the $A_{l\mu}^{SS}(\boldsymbol{\tau})$ parameters. In the second step, the Fourier coefficients of the ODF were obtained for the lowest l values using the $A_{l\mu}^{SS}(\boldsymbol{\tau})$ parameters obtained from different beam directions.

Two different approaches were proposed to obtain the first Fourier coefficients of the ODF. In the first approach, the beam direction was rotated to align the (200) pole at the center of the pole figure, with the inversion model assuming cylindrical or orthorhombic sample symmetry. This approach yielded good results, particularly for higher-symmetry cases. In the second approach, the texture was assumed to be fiber-like, with the fiber axis direction in the sample reference system being fitted from the experimental data. This method was able to accurately identify the fiber axis direction and capture the main features of the texture.

The current inversion method for texture evaluation assumes a uniform texture of the sample. However, this does not mean that the method cannot be applied to samples with texture gradients. By rotating the sample normal to the direction of the texture gradient, the method can still be used to analyze each vertical section of the sample separately. This way, each section can be treated under the requirements of the method, enabling determination of the texture for the whole sample.

Acknowledgements

We would like to express our gratitude to reviewer Dr Pingguang Xu of the Japan Atomic Energy Agency for the meticulous effort put into their work which has significantly enhanced the readability of this article.

Funding information

Partial funding was provided by CONICET and by the Board of the Swiss Federal Institutes of Technology via funding from the Strategic Focus Area Advanced Manufacturing program.

References

Artioli, G. (2007). *Appl. Phys. A*, **89**, 899–908.
Bunge, H. J. (1982). *Texture Analysis in Materials Science: Mathematical Methods*. London: Butterworths.
Carminati, C., Strobl, M., Minniti, T., Boillat, P., Hovind, J., Morgano, M., Holm Rod, T., Polatidis, E., Valsecchi, J., Mannes, D., Kockelmann, W. & Kaestner, A. (2020). *J. Appl. Cryst.* **53**, 188–196.
Dessieux, L. L., Stoica, A. D., Bingham, P. R., An, K., Frost, M. J. & Bilheux, H. Z. (2019). *Nucl. Instrum. Methods Phys. Res. B*, **459**, 166–178.
Dollase, W. A. (1986). *J. Appl. Cryst.* **19**, 267–272.
Granada, J. R. (1984). *Z. Naturforsch. A*, **39**, 1160–1167.
Hielscher, R. & Schaeben, H. (2008). *J. Appl. Cryst.* **41**, 1024–1037.
Laliena, V., Vicente-Álvarez, M. Á. & Campo, J. (2020). *J. Appl. Cryst.* **53**, 512–529.
Luzin, V. & Brokmeier, H. G. (2002). *Mater. Sci. Forum*, **408–412**, 191–196.
Malamud, F. (2016). PhD thesis, Instituto Balseiro, Rio Negro, Argentina.
Malamud, F. & Santisteban, J. R. (2016). *J. Appl. Cryst.* **49**, 348–365.
Malamud, F., Santisteban, J. R., Vicente Alvarez, M. A., Bolmaro, R., Kelleher, J., Kabra, S. & Kockelmann, W. (2014). *J. Appl. Cryst.* **47**, 1337–1354.
Malamud, F., Santisteban, J. R., Vicente Alvarez, M. A., Busi, M., Polatidis, E. & Strobl, M. (2023). *J. Appl. Cryst.* **56**, 143–154.
Morris, R. R. (1995). *Texture Microstruct.* **24**, 221–224.
Muggli, J. (1972). *J. Appl. Math. Phys. (ZAMP)*, **23**, 311–317.
Onuki, Y., Hoshikawa, A., Sato, S., Xu, P. G., Ishigaki, T., Saito, Y., Todoroki, H. & Hayashi, M. (2016). *J. Appl. Cryst.* **49**, 1579–1584.
Peterson, N. E., Einhorn, J. R., Fancher, C. M., Bunn, J. R., Payzant, E. A. & Agnew, S. R. (2021). *J. Appl. Cryst.* **54**, 867–877.
Santisteban, J. R., Daymond, M. R., James, J. A. & Edwards, L. (2006). *J. Appl. Cryst.* **39**, 812–825.
Santisteban, J. R., Edwards, L., Steuwer, A. & Withers, P. J. (2001). *J. Appl. Cryst.* **34**, 289–297.
Santisteban, J. R., Vicente-Alvarez, M. A., Vizcaino, P., Banchik, A. D., Vogel, S. C., Tremsin, A. S., Vallerga, J. V., McPhate, J. B., Lehmann, E. & Kockelmann, W. (2012). *J. Nucl. Mater.* **425**, 218–227.
Sato, H., Kamiyama, T. & Kiyanagi, Y. (2011). *Mater. Trans.* **52**, 1294–1302.
Sato, H., Sato, M., Su, Y., Shinohara, T. & Kamiyama, T. (2021). *ISIJ Int.* **61**, 1584–1593.
Sears, V. F. & Shelley, S. A. (1991). *Acta Cryst.* A**47**, 441–446.
Su, Y., Oikawa, K., Harjo, S., Shinohara, T., Kai, T., Harada, M., Hiroi, K., Zhang, S., Parker, J. D., Sato, H., Shiota, Y., Kiyanagi, Y. & Tomota, Y. (2016). *Mater. Sci. Eng. A*, **675**, 19–31.
Su, Y., Oikawa, K., Shinohara, T., Kai, T., Horino, T., Idohara, O., Misaka, Y. & Tomota, Y. (2021). *Sci. Rep.* **11**, 4155.
Takajo, S. & Vogel, S. C. (2018). *J. Appl. Cryst.* **51**, 895–900.
Vicente Alvarez, M. A., Laliena, V., Malamud, F., Campo, J. & Santisteban, J. (2021). *J. Appl. Cryst.* **54**, 903–913.

Vogel, S. (2000). PhD thesis, Christian-Albrechts Universität zu Kiel, Germany.
Watanabe, K., Minniti, T., Sato, H., Tremsin, A. S., Kockelmann, W., Dalgliesh, R. & Kiyanagi, Y. (2019). *Nucl. Instrum. Methods Phys. Res. A*, **944**, 162532.
Wensrich, C. M. J. N., Hendriks, M. H. & Meylan, M. H. (2016). *Strain*, **52**, 80–87.
Woracek, R., Penumadu, D., Kardjilov, N., Hilger, A., Boin, M., Banhart, J. & Manke, I. (2014). *Adv. Mater.* **26**, 4069–4073.
Woracek, R., Santisteban, J., Fedrigo, A. & Strobl, M. (2018). *Nucl. Instrum. Methods Phys. Res. A*, **878**, 141–158.
Xu, P. G., Harjo, S., Ojima, M., Suzuki, H., Ito, T., Gong, W., Vogel, S. C., Inoue, J., Tomota, Y., Aizawa, K. & Akita, K. (2018). *J. Appl. Cryst.* **51**, 746–760.